Article:
Collins, J., Taylor, M., Scarlett, A.L. et al. (2 more authors) (2024) Prior austenite grain measurement: A direct comparison of EBSD reconstruction, thermal etching and chemical etching. Materials Characterization, 208. 113656. ISSN 1044-5803

https://doi.org/10.1016/j.matchar.2024.113656

Materials Characterization 208 (2024) 113656

Contents lists available at ScienceDirect

Materials Characterization

journal homepage: www.elsevier.com/locate/matchar

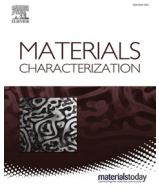

Prior austenite grain measurement: A direct comparison of EBSD reconstruction, thermal etching and chemical etching

J. Collins [a,*], M. Taylor [a], A.L. Scarlett [b], E.J. Palmiere [b], E.J. Pickering [a,c]

[a] Department of Materials, The University of Manchester, Oxford Road, Manchester M13 9PL, UK
[b] Department of Materials Science and Engineering, The University of Sheffield, Sheffield S1 3JD, UK
[c] Henry Royce Institute, Oxford Road, Manchester M13 9PL, UK

ARTICLE INFO

Keywords:
Steel
PAG
Thermal etching
Picric acid
EBSD
Parent reconstruction

ABSTRACT

It is well known that the prior austenite grain (PAG) microstructure of steels has a significant impact on their microstructure evolution and mechanical properties. Many PAG measuring techniques have been developed over many decades, with the effectiveness of each varying alloy-to-alloy. Some of the more common techniques, specifically for bainitic and martensitic grades, are thermal etching and picric acid etching, which both involve the preferential etching of PAG boundaries in order to reveal the austenitic microstructure. More recently, parent grain reconstruction techniques using EBSD (electron backscatter diffraction) mapping have shown good promise in recreating PAG microstructures from BCC-FCC orientation relationships, and can now be deployed at speed with the advent of rapid detectors (1000s of pixels per second). This study aims to compare the accuracy and relative advantages/disadvantages of picric acid etching, thermal etching and EBSD reconstruction methods. A TESCAN and NewTec In-Situ Testing (TANIST) capability was used to directly observe and measure the true high-temperature PAG structure during the austenitisation of SA-540 B24 low alloy steel. These high-temperature PAG measurements were then compared to measurements from the same area obtained using thermal etching, picric acid etching and EBSD parent grain reconstructions after quenching to room temperature. Reconstructing the parent austenite grains from EBSD data resulted in the closest measurement of PAG size. PAG boundaries were delineated well by thermal etching but surface effects (such as surface relief and ghost traces) created complexities when identifying the exact position of boundaries. Picric acid etching, which produced the least accurate measurement, was found to reveal PAG boundaries well, however it was limited by its ability to sufficiently etch annealing twin boundaries and its susceptibility to microsegregational effects. EBSD reconstruction and thermal etching were more consistent at reconstructing/revealing these boundaries, although inaccuracies with the techniques were still observed.

1. Introduction

A quantitative analysis of the prior austenite grain (PAG) structure of steels is greatly desired when attempting to understand and predict the microstructural and mechanical behaviour of an alloy. PAG size has a direct effect on strength through the Hall-Petch effect (by constraining the scale of transformed microstructures) [1,2] or indirectly by altering the transformation kinetics leading to the formation of micro-constituents with varying strengths. Other mechanical properties, such as toughness, can also be significantly affected by these PAG size effects.

There is an abundance of techniques that can be used to measure and quantify the PAG structure of steels. These techniques can be broken down into either: (i) direct procedures - where the austenite is directly observed at high temperature (i.e., above the Ac_3) usually via a high temperature microscope, or (ii) indirect procedures - where austenite grains are able to be imaged at room temperature by revealing grain boundaries through either heat treatment or other metallographic techniques. The most commonly used techniques generally reside within the latter as they are much simpler and easier to conduct. Microstructural observation at high temperature is far more complex than at room temperature and, as a result, requires more precise and sophisticated equipment, as well as a microscopist proficient in the technique.

* Corresponding author.
E-mail addresses: joshua.collins@manchester.ac.uk (J. Collins), mark.taylor-5@manchester.ac.uk (M. Taylor), ascarlett1@sheffield.ac.uk (A.L. Scarlett), e.j.palmiere@sheffield.ac.uk (E.J. Palmiere), ed.pickering@manchester.ac.uk (E.J. Pickering).

https://doi.org/10.1016/j.matchar.2024.113656
Received 29 November 2023; Received in revised form 8 January 2024; Accepted 9 January 2024
Available online 11 January 2024

Two of the more common indirect techniques used for bainitic and martensitic steels are thermal etching and chemical etching, although thermal etching has also been shown to be successful for ferritic and pearlitic grades [3–5]. Both techniques rely on the preferential etching of PAG boundaries in order to reveal the PAG structure. In thermal etching, this is achieved by heating a polished sample surface above its Ac_3 temperature (i.e., $\alpha + \gamma \rightarrow \gamma$), usually under vacuum or inert atmosphere in order to protect the surface. Thermal grooves then form at austenite grain boundaries due to surface tension effects and matter transport [6]. These grooves are then retained and can be imaged when cooled to room temperature. Many studies have successfully used thermal etching to reveal PAG boundaries [3–5,7], however the technique is not without its limitations. A re-austenitisation is required in order to first develop the grooves, thus, in many cases, limiting the technique to exploratory studies rather than forensic analysis of a sample in its as-received state. Furthermore, sufficient austenitisation times and temperatures are required to develop substantial grooving so that PAG boundaries can be identified, with exact parameters likely varying between alloys. Finally, the thermally etched interface is often plagued with multiple grooves left over from grain boundary migration often leading to inaccurate measurements of PAG size. These traces of prior boundary were attributed, by Mullins [6], to be a result of spasmodic boundary movement. A study by Andres et al. [4] observed that these "ghost traces" were more abundant at higher austenitisation times and temperatures when grain boundary mobility is slowed by larger PAG sizes and deepened grooving.

Chemical etching utilises an acid etchant to attack and reveal PAG boundaries. Early techniques used Vilella's reagent - a mixture of picric acid, HCl and ethanol - to reveal PAG boundaries. Vilella's Reagent is still used to etch medium carbon steels, although it is more commonly used to reveal carbides and microstructures [8–10]. Later, Bechet and Beaujard [11] demonstrated the use of saturated picric acid solution to successfully reveal PAG boundaries. Their technique involved using 0.5% sodium alkyl sulfonate (more readily known as 'Teepol') as a wetting agent and has been used as the basis for many other successful etchants since then. The mechanism of chemical etching relies on the segregation of impurities to PAG boundaries to ensure an etch of the boundary but not the matrix [12]. Capus [13] showed that PAG boundary etching using picric acid was related to the presence of impurity elements such as P. Moreover, Ücisik et al. [14] demonstrated an improved PAG boundary etching after tempering their steel, which has been experimentally shown to increase grain boundary impurity segregation [15]. For picric acid etching there is a high dependency on the wetting agent used. Recent work by Thackray et al. [16] determined that sodium dodecyl sulfonate was an optimum wetting agent for low and medium-carbon steels, and sodium dodecylbenzene sulfonate was better for high-carbon steels. Thackray et al. also used 'dummy' samples to mature the picric acid solution (i.e., reduce the strength of the acid) before etching and to help remove the reliance on polishing back samples to limit visibility of martensitic structures. Also recently, Rodriguez-Galeano et al. [17] proposed a revised method for low-alloy steels using a combination of sodium dodecyl sulfate and HCl. In addition to a suitable wetting agent, the solvent is also critical. Barraclough [18] found that alcohol did not produce ideal results and that water or ether was more appropriate. Barraclough also found that heating the solution to around 85 °C improved results. Lightly polishing the etched surface was also found to help differentiate between etched PAG boundaries and non-PAG boundary structures.

Since the 1990s, orientation mapping techniques, such as electron backscatter diffraction (EBSD), have made it possible to observe the crystallographic structure of parent phase microstructures by understanding transformation crystallography. EBSD is a microstructural imaging technique that can be used to obtain material crystallographic data (e.g., crystal structure and orientation) across large areas and to a high resolution [19]. Since the adoption of EBSD, it was quickly established that the crystallographic data obtained could also be used to analyse parent microstructures [20]. By understanding the orientation relationship (OR) between parent (e.g., FCC austenite) and child (e.g., BCC martensite or bainite) the crystallographic status of the prior austenitic microstructure can be obtained from the orientation mapping of the child grain structure [21]. The most frequent ORs used to describe the phase transformation between FCC and BCC crystals are the Kurdjumov-Sachs (K—S) OR [22] and the Nishiyama-Wasserman (N—W) OR [23]. These child-to-parent reconstructions can be quickly and easily performed using software packages such as Oxford Instruments (OI) AZtecCrystal [24] and MTEX [25]. Many parent grain reconstruction algorithms can be divided into two distinct approaches; grain graph (e.g., [26–28]) and nucleation-growth (e.g., [21,29,30]). The grain graph approach works by assigning each grain boundary (edge) a probability of belonging to a common parent grain. Child grains (nodes) that are likely to belong to the same parent grain are then clustered together and reconstructed. The nucleation-growth approach works by identifying local child grains with a common parent orientation variant, coalesces them into one group (a nucleus) and allows them to grow into the surrounding parent phase. A voting mechanism is then used to determine the likely parent orientation variant from the participating child grains [31]. AZtecCrystal reconstruction software adopts a nucleation-growth approach and is based off the work published by Huang et al. [30]. MTEX, on the other hand, provides the user with both grain-graph and nucleation-growth approaches [32]. Moreover, Hielscher et al. [31] recently developed a hybrid variant graph approach, which combines the advantages of both the grain graph and nucleation-growth approaches, which has also been implemented into MTEX. Many EBSD reconstruction techniques have been shown to successfully measure the PAG size of steels, however they are still limited by a number of factors. The primary factor is the quality of the child EBSD map. Any measurement errors in the initial EBSD map will ultimately lead to errors in the resulting reconstruction. Another limitation of current EBSD reconstruction algorithms is their ability to accurately reconstruct annealing twin boundaries which, due to their crystal symmetries, can be difficult to isolate [30,32–34].

It is difficult to assess which of the techniques described above is most appropriate for revealing and measuring austenite grain size. Previous work by Andrés et al. [3] compared the applicability and reliability of thermal and chemical etching PAG measurement techniques. They found that for medium carbon, microalloyed steels, thermal etching was a far more reliable technique than the various chemical etching techniques at the time. Subsequent work by the same authors [4] then outlined the advantages and disadvantages of the thermal etching method. Since then, improvements have been made to picric etching techniques [16,17] which showed good success for low, medium and high carbon steels. To the authors' knowledge, a comparison between these 'traditional' PAG revealing techniques and the newer reconstruction methods has yet to be conducted. Picric etching methods have been used to help validate reconstructed microstructures in recent studies [27,35] but a direct comparison of their accuracies was not assessed.

This study aims to directly assess the accuracy of three PAG measurement techniques: thermal etching, chemical etching and parent grain reconstructions, by direct comparison with the same region-of-interest (ROI). Importantly, we begin by first observing the high temperature, austenitic microstructure immediately before quenching. This is achieved by using a hot-stage electron microscope to perform EBSD measurements during an austenitisation and quench treatment of SA-540 B24 low alloy steel. This high-temperature PAG microstructure is then directly compared with measurements of the same ROI obtained after cooling using thermal etching, picric acid etching and EBSD reconstruction. The accuracy, applicability and resilience of each technique will be evaluated and considered within this assessment. It is noted that direct assessments with the 'true' austenitic microstructure have previously been used to help validate reconstruction algorithms [28,36] but a critical comparison between other techniques using the same ROI has not yet been conducted.

2. Material and methods

The composition of the SA-540 steel alloy examined is presented in Table 1. The alloy composition was measured using optical emission spectroscopy (OES). A TANIST (TESCAN And NewTec In-Situ Testing) custom-built system, consisting of a TESCAN Clara SEM with an OI Symmetry EBSD detector, was used to observe microstructural developments during and after steel austenitisation. A small cylinder of material (4 mm diameter, 2 mm length) was first extracted along the material forging direction using a combination of electric discharge machining (EDM) and precision cutting. A circular face of this cylinder was then ground and polished to a 0.06 μm finish, first using diamond paste and then a colloidal silica suspension.

Figure 1 shows the temperature-time curve for the heating stage experiment. The cylindrical sample was mounted to a heating stage using conductive carbon paste and heated to 700 °C, just below the temperature at which austenite was to form. Heating was conducted in 50 °C steps in order to control degassing and beam focussing. An average heating rate of around 0.6°Cs^{-1} was achieved during this step. After reaching 700 °C, the sample was then slowly heated to 920 °C, in 20 °C steps and averaging a heating rate of around 0.1°Cs^{-1}. At each 20 °C interval, EBSD observations of the ROI were taken to monitor the transformation of BCC to FCC. EBSD measurements were recorded using OI AZtec software (version 6.0). A 20 kV accelerating voltage and 30 nA beam current were used throughout the experiment and during EBSD and secondary electron (SE) image collection. Once fully FCC, the sample was held at 920 °C for approximately 1.8 h, all while the austenitic microstructure of the ROI was monitored. In the last 5 min of the hold, the sample temperature was raised to 940 °C in an attempt to increase austenite grain growth (to improve their viewability for thermal and chemical etching). At the end of the 940 °C hold (see point 'a' in Fig. 1), a final EBSD map was measured at a step size of 1 μm and the sample was left to cool under vacuum to room temperature. It is noted that no temperature data was recorded during the cooling step. Once the sample had reached 30 °C (see point 'b' in Fig. 2), an EBSD map of the ROI (now martensitic BCC) was acquired (step size = 0.3 μm) as well as an SE map of the thermally etched surface. EDS (electron-dispersive x-ray spectroscopy) analysis was also conducted across the ROI, using an OI Ultim Max 170 EDS detector, in order to measure potential solute variations.

Samples were subjected to a minimal 0.25 μm polish in order to remove the thermal etch on the surface. The polished surface was then chemically etched using picric acid to reveal PAG boundaries. It was assumed that the amount of material removed during polishing was very small and that the newly revealed microstructure was the same as the microstructure observed at high temperature (indeed, this was evident from the resulting micrographs). The saturated picric acid solution was made from an addition of 4.5 g of picric acid to a beaker of deionized water, with 1.15 g of sodium dodecyl sulfate and 5 drops of HCl. A total of 4 'dummy' samples of low-alloy steel were added for 5 min each, for a total of 20 min to mature the etchant. For reproducibility, the colour of the etchant should be a dark orange, without turning brown. Once matured, the sample was submerged for around 4 min followed by a brief hand polish with 0.06 μm colloidal silica. The same ROI on the sample surface was then relocated and imaged using SE imaging using an FEI Magellan 400 SEM. It should also be noted that there will likely be some small discrepancies between the high temperature austenite grain map and the chemically etched surface due to small misalignments during the relocation of the ROI. To characterise the cooling transformation, the sample surface was gently polished back for a second time, to remove the picric etched surface, and re-etched using 2% Nital acid. The as-cooled microstructure was then imaged using an FEI Magellan 400 SEM. A similar procedure was also done to prepare the sample cross-section for SE imaging as well as EBSD and EDS mapping. Details of the conditions used are provided in the supplementary material of this work. To aid the characterisation of microstructures, a Matsuzawa MMT-X7A microhardness indenter was used to collect a total of 6 hardness measurements (1 kgf, over a dwell of 10 s) of the bulk, cross-section.

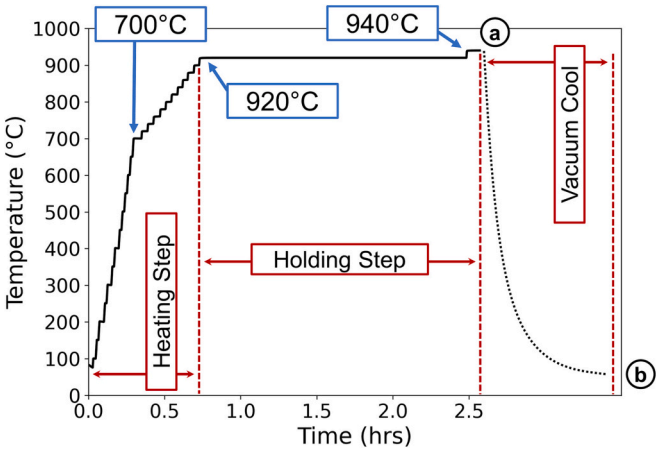

Fig. 1. The measured temperature-time curve for the heating stage experiment. The vacuum cooling step has been included here but as a black dotted line to indicate that temperature measurements were not taken during this step. Points 'a' and 'b' refer to points when the microstructure was measured. The high-temperature FCC EBSD was acquired at point 'a'. The thermally etched surface, room-temperature BCC EBSD and picric acid etched surface were measured at point 'b'.

Parent grain reconstructions from the EBSD data were conducted using OI AZtecCrystal software (version 3.1). The BCC EBSD map, which can be view in Supplementary Fig. S-1, was first cleaned to remove any potentially mis-indexed pixels (i.e., a misrepresented orientation) and any non-indexed pixels using the AZtecCrystal "Clean Up" tool. A mis-indexed pixel, termed a "wild spike", is determined as a pixel with an orientation that is completely different to its surrounding pixels. The wild spike is then replaced with a more suitable orientation based off the surrounding pixels. Non-indexed pixels are replaced by growing the surrounding, indexed pixels into the non-indexed spaces. A N—W OR [23] was selected as the best approximated OR for SA-540. Two training regions were chosen for OR refinement from the child EBSD map. Regions were selected within a twinned PAG and care was taken not to cross austenite boundaries so as not to mix orientation relationships. The training regions used can be viewed in Supplementary Fig. S-1. Different parameters were tested for optimal parent reconstruction. The final parameters chosen are presented in Table 2. The size of the reconstructed austenite grains were measured using AZtecCrystal and an average area-weighted equivalent circle diameter ($\overline{d}$) and area-weighted standard deviation ($\overline{\sigma}$) were calculated. The equations used to calculate these values are provided in Appendix A. It is noted that measured austenite grain sizes from each technique will be presented in the format $\overline{d} \pm \overline{\sigma}$, where the standard deviation, $\overline{\sigma}$ is a measure of size distribution and not a measure of error.

The revealed PAG boundaries from thermal and chemical etching were first isolated from the original SE images by tracing over the

Table 1
Chemical composition (wt%) of the SA-540 alloy examined.

C	Si	Mn	Ni	Cr	Mo	Cu	Al	V	Ti	Nb	S	N
0.40	0.26	0.75	1.81	0.86	0.32	0.08	0.031	0.01	0.01	0.01	0.008	0.008

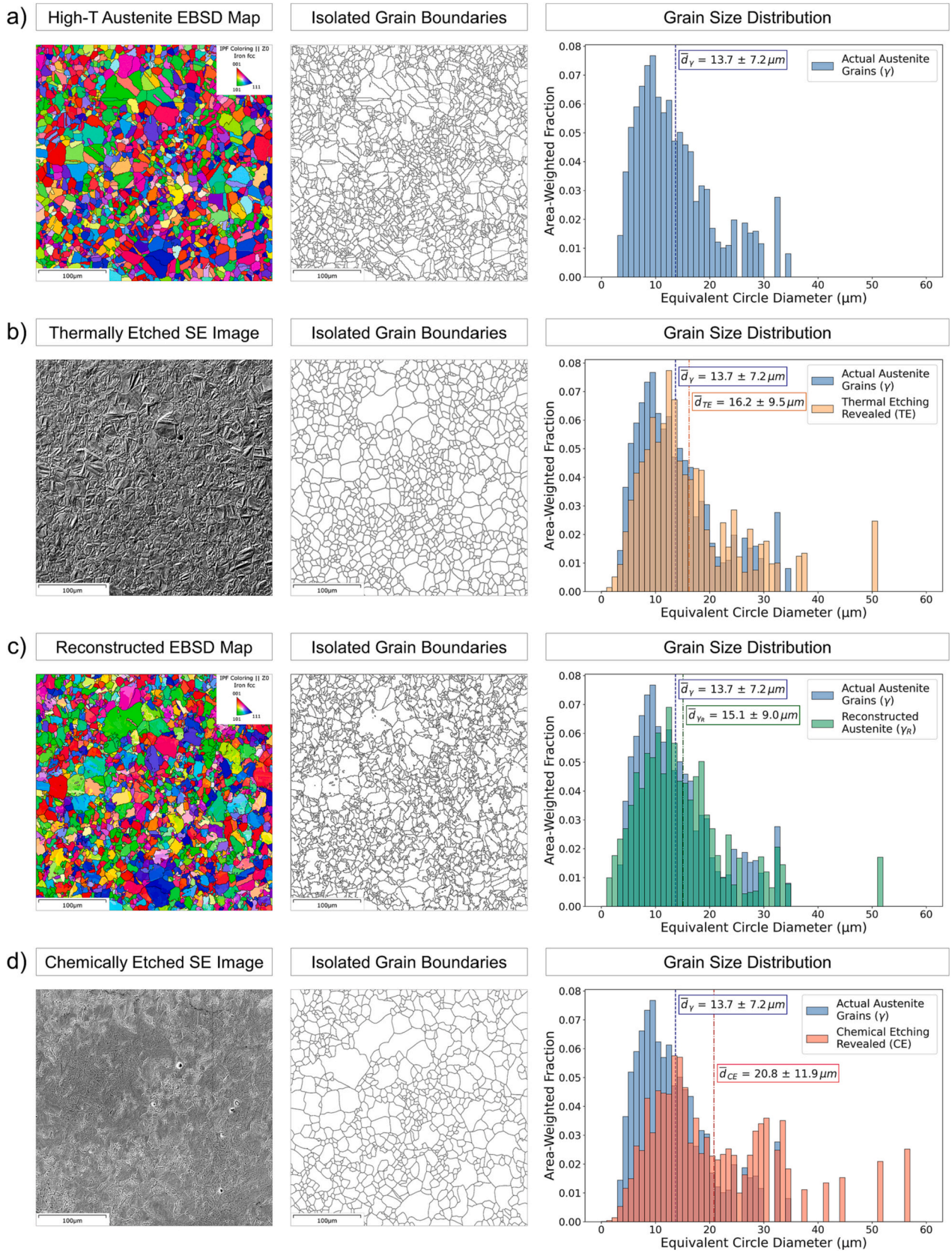

Fig. 2. Austenite grain microstructures measured/revealed using (a) high-temperature, in-situ EBSD at 940 °C, (b) thermal etching, (c) parent grain reconstruction, and (d) chemical (picric acid) etching. Measurements of (b), (c) and (d) were acquired at room temperature after cooling from 940 °C. The measured/revealed austenitic microstructures are displayed next to their isolated grain boundaries and the area-weighted histograms of the measured equivalent circle diameters.

Table 2
Optimum parameters selected for AZtecCrystal parent grain reconstruction.

Child thresh (°)	Window size (pix)	Step width (%)	Voting thresh (°)	Parent thresh (°)
2.5	25	25	5	10

boundaries. This produced a grain boundary map of both surfaces without the visual noise of the non-boundary regions. To analyse these maps, a Python code was written to automatically measure the size of each PAG. The code utilises the SciPy [37] and scikit-image [38] libraries in order to identify and measure grains in the grain boundary maps. The code has been published and made available on GitHub [39].

3. Results

The results for each technique are presented in Fig. 2 and each show; (i) the observed austenitic microstructure, obtained using either EBSD or SE imaging, within the ROI, (ii) the isolated austenite grain boundaries, and (iii) an area-weighted histogram of the measured equivalent circle grain diameters. For better comparison, the histogram of the 'true', high-temperature austenite grain sizes (i.e., Fig. 2a) has been superimposed onto each of the other histograms. The average area-weighted mean, $\overline{d}$, and standard deviation are also displayed on each histogram. Table 3 presents the calculated $\overline{d}$ values for each technique, as well as a percentage (%) difference between the $\overline{d}$ measured from the high temperature austenite map. The ASTM grain size was also calculated from $\overline{d}$ using the expression provided in Appendix B, and is also displayed in Table 3.

The austenitic grain microstructure observed at high temperature, in Fig. 2a, shows that a bimodal distribution of grains exists in the steel. The weighted majority of austenite grains lie below 20 μm in size, with a maxima measured between 9 and 10 μm. A second maxima, however, is observed within the histogram between 32 and 33 μm, although the sample size of grains this large is significantly reduced. The area-weighted average equivalent circle diameter of the austenite grains, $\overline{d}_{\gamma}$, was calculated to be 13.7 ± 7.2 μm. The bimodal distribution of grains can be observed in the measured EBSD map, where two regions of larger austenite grains are present just above the centre and on the right hand side of the map. EDS analysis suggests that this bimodal distribution of grain sizes is caused by the presence of chemical microsegregation within the examined steel. EDS maps, normalised using their average compositions, measured for Cr, Mn, Mo, Ni, Si and Al can be viewed in Supplementary Fig. S-2 and show a distinct variation in Cr across the ROI. Variations in Ni and Mo can also be identified in the same pattern as Cr, however are much less distinct. Indeed, the larger grains appear to follow the areas enriched in solute (i.e., the interdendritic regions), suggesting a correlation between austenite grain growth and chemical microsegregation. Further analysis showed that the majority of austenite grains are broken up by annealing twins. The boundaries at these twins were measured in AZtecCrystal to have a disorientation of around 60° about the ⟨111⟩ axis. Although present across the entire microstructure, these twins are more noticeable in the larger austenite grains.

Table 3
A table showing the calculated area-weighted average equivalent circular diameter ($\overline{d}$) of the high temperature EBSD map, the thermally etched surface, the parent grain reconstructed map, and the chemically etched surface, where the calculation of $\overline{d}$ includes both austenite and twin boundaries. The percentage (%.) difference from the 'true', high temperature grains, as well as the ASTM grain size of each measurement were also calculated.

Technique	$\overline{d}$ (μm)	%. Difference	ASTM grain size
High temperature EBSD	13.7 ± 7.2	–	9.4
Thermal etching	16.2 ± 9.5	+ 18.2%	9.0
Parent reconstruction	15.1 ± 9.0	+ 10.2%	9.2
Chemical etching	20.8 ± 11.9	+ 51.8%	8.2

Observations of the thermally etched surface in Fig. 2b reveals a similar austenitic grain structure to that measured at high temperature. The thermal grooving is deep and outlines the PAG boundaries well. Examination reveals some, but infrequent, ghost traces, although many grains contain large, intragranular distortions which are likely a result of the strain induced by the FCC to BCC transformation that occurred on cooling. When isolating the grain boundaries, the thermally etched microstructure also appears to be bimodal, however the distribution is skewed to higher grain sizes. Many annealing twin boundaries were not adequately revealed by the thermal etching process. Thus, many grains, which were broken up into smaller counterparts by twin boundaries, were measured to be significantly larger than those measured with high-temperature EBSD. These discrepancies resulted in a measured average area-weighted diameter, $\overline{d}_{TE}$, of 16.2 ± 9.5 μm from the thermally etched surface, thereby causing an overestimation by 18.2% in comparison to the 'true', high-temperature measurement.

The austenite grain map reconstructed from the room temperature BCC microstructure, in Fig. 2c, visually resembles the actual austenite grain structure very well. Analysis of the as-cooled microstructure revealed that the sample surface formed a mixture of bainite and martensite, with some martensite appearing autotempered (owing to the presence of carbides). This result was unexpected as it was believed that the SA-540 sample would cool sufficiently fast to not form significant amounts of bainite. An SE image showing these structures is presented in Supplementary Fig. S-3a. Notably, a far greater fraction of martensite was observed in the regions measured to be enriched in solute. The microstructure of the bulk, cross-section was also examined (see Supplementary Fig. S-3b) and shows a similar microstructure to the surface. Both bainite and martensite were found to reconstruct into the 'true' austenitic microstructure well. Some discrepancies were observed however, primarily when the austenite grains are broken up by annealing twins. In most cases this has resulted in the reconstruction of irregular and ambiguous grain boundaries. In some cases however, this has resulted in wrongly reconstructed grains and misidentified austenite orientations. Nevertheless, AZtecCrystal's parent grain reconstruction produced a good estimation of the PAG microstructure. The average area-weighted diameter of the reconstructed map, $\overline{d}_{\gamma_R}$, was measured to be 15.1 ± 9.0 μm, which is only 10.2% higher than the high-temperature austenite grain measurement. The grain size distribution of the reconstructed PAGs is very similar to the 'true' grain distribution and is shown to be somewhat bimodal. The reconstructed map predicts a far higher density of smaller grains than the actual austenitic structure, however. These smaller grains appear to be a symptom of the reconstruction algorithm, specifically when attempting to identify annealing twin boundaries. Many twin boundaries were partially reconstructed and segmented into smaller parts, leading to an increased measurement of smaller PAGs. Equally, this higher density of smaller grains could have been influenced by the different step sizes used when collecting the high temperature and room temperature EBSD maps (1 μm and 0.3 μm respectively). Moreover, the reconstructed map, like the thermal etched measurements, shows a large, outlying grain at 51 μm. In the actual austenitic microstructure (Fig. 2a) this grain in question is segmented into smaller parts by multiple annealing twins. The reconstruction, however, was not able to accurately capture these twins and the grain was measured to be far larger, producing a skew in the grain size distribution.

Etching SA-540 steel with picric acid successfully revealed the prior austenite microstructure across the majority of the ROI (see Fig. 2d). Nevertheless, the accuracy of the technique appears to be affected by the chemical segregation within the material. Interdendritic regions, i.e., the regions showing an enrichment of Cr, Ni and Mo in Supplementary Fig. S-2, appear to have etched quicker than those with reduced solute concentrations. As a consequence, this made the identification of PAG

boundaries within these regions more difficult. The average area-weighted diameter, $\overline{d}_{CE}$, was measured at 20.8 ± 11.9 μm from the chemically etched grains. This value is around 51.8% higher than the actual austenite grain size and this large disparity was likely a result of the difficulties in measuring the over-etched regions. Equally, the majority of the annealing twins measured in the actual austenitic grain microstructure were not revealed by the picric etching and were not considered in the final measurement. Because of these effects, the grain size distribution was greatly skewed to higher grain sizes.

4. Discussion

Comparison of the techniques used to measure the PAG structure of SA-540 material shows that all three methods over-estimate the average austenite grain size when compared to the 'true' microstructure measured at high temperature. Parent grain reconstruction produced the most accurate measurement of PAG size at 15.1 μm, however the position and coherency of some grain boundaries were lost during the reconstruction. Thermal etching produced the next most accurate measurement at 16.2 μm and chemical etching produced the least accurate measurement at 20.8 μm. Both etching techniques showed good accuracy in locating the exact position of FCC grain boundaries, but showed difficulty in revealing annealing twin boundaries. It is noted that small changes in the relative position of parent grains will have occurred between the high temperature hold and cooling to room temperature, due to sample contraction and microstructural adjustments. Because of this, there will always be a small error between the 'true', high-temperature austenite measurements and the measurements taken at room temperature. The condition of the analysed surfaces played an important role in each technique's ability to accurately measure the prior austenitic microstructure. Analysis of the thermally etched surface was impacted by the presence of surface relief and ghost traces. Inter-dendritic regions of the chemically etched surface showed an increased etching effect, making some PAGs impossible to identify. These same regions also showed a notable decrease in diffraction pattern quality during the collection of the room temperature EBSD map. This is best visualised in the EBSD band contrast (i.e., diffraction pattern intensity) map of the room temperature, BCC microstructure in Supplementary Fig. S-1a. The limitations of each technique will be discussed further in the sections below.

4.1. Impact of annealing twins

The EBSD map of the high-temperature, austenitic microstructure shows the presence of a significant number of annealing twins. These types of twins commonly form in FCC metals and alloys with low-to-medium stacking fault energies [40] and break up austenite grains into smaller parts. The ASTM standard E112–10 [41] states that annealing twin boundaries should be ignored when measuring the size of PAGs. These boundaries, however, were recently observed to act as like austenite boundaries, with respect to martensite and bainite impingement during cooling, in a recent study by Taylor et al. [34]. In situ observations of the austenite transformation showed that both martensitic laths and bainitic sheaves did not cross twin boundaries, meaning that they were either impeded by or nucleated from them. It is therefore assumed, in this work, that a twin boundary acts equivalently to an austenite grain boundary and splits the austenite into two independent grains. As a consequence, annealing twins will reduce the average PAG size of the system. A more appropriate way of quantifying the parent microstructure therefore might be the measurement of the amount of relative grain boundary surface per unit volume, S_V [42], which would allow high angle, low angle and twin boundaries to all be accounted for. For consistency with other works [3,7,34] however, here the austenite microstructure has been defined in this work by a measurement of grain size, where grain size considers the presence of twin boundaries.

All three techniques examined show difficulty in identifying annealing twin boundaries as independent FCC boundaries. The misorientation between two twinned FCC crystals is a 60° rotation about a ⟨111⟩ axis, making it distinct from regular FCC boundaries. By removing these twin boundaries in AZtecCrystal, the austenite grain boundaries in the high temperature austenite map were isolated. An austenite grain containing multiple twins was selected using this method and is presented in Fig. 3. The same grain-of-interest (GOI) was then isolated from the BCC EBSD map, the reconstructed austenite map, the thermally etched surface and the chemically etched surface. These are also presented in Fig. 3. Observations of the high temperature austenite microstructure show that the twinned GOI is separated into five distinct regions by the introduction of four twin boundaries. Each annealing twin has been labelled in Fig. 3a from 1 to 4. Arrows indicating the position of each of these boundaries have been superimposed on the GOI and duplicated for each technique's representation of that grain. This GOI will be used to help visualise and discuss each technique's ability to delineate twin boundaries. Although only one austenite grain is discussed, it is illustrative of trends seen across each of the microstructures revealed/reconstructed by each technique.

The BCC structure, measured via the room temperature EBSD (Fig. 3b), can be seen to roughly follow each of these regions. Both low angle (2–10°) and high angle (>10°) BCC boundaries are observed to follow the exact positions of these twin boundaries. Interestingly, the BCC grains on the left-hand-side on the GOI do not perfectly match with the high temperature grain. It is believed that this discrepancy is due to a mis-indexing of the child EBSD map, as the additional PAG area is not revealed by thermal or chemical etching techniques (see Fig. 3d and 3e). This mis-indexing could have been caused by the strain induced by the BCC transformation and the resultant surface relief at the sample surface. Nevertheless, the position of the annealing twin boundaries appear unchanged. The reconstructed GOI in Fig. 3c shows that AZtecCrystal software was somewhat successful in its reconstruction of the annealing twins. Refining the OR to more accurately represent the actual OR of the EBSD map, rather than using the fixed N—W OR, showed a significant improvement in the reconstruction of twins. The importance of OR refinement for parent reconstructions is demonstrated well in the work by Miyamoto et al. [33]. Comparing Fig. 3a to 3c shows that twin number 1 was reconstructed successfully, however twins 2 and 3 were only partially reconstructed and twin number 4 appears to have been lost and instead incorporated as a part of twin 3. The difficulty in reconstructing annealing twin boundaries has been a common problem since the first martensite-austenite reconstructions by Cayron [21]. Many reconstruction algorithms have struggled with accurately reconstructing annealing twins in steels [30,32,33]. When considering the K—S OR, each {111} FCC habit plane can produce six different BCC orientations (or variants) [43]. This would be reduced to three orientations for the N—W OR. The {1 1 1} twinning planes will be parallel and therefore, either side of the twin, will share six (or three) identical BCC variants. Moreover, austenite twin boundaries tend to share common BCC variants in order to minimise transformation strain [44] which will add further ambiguity to the location of twin boundaries. Huang et al. [30] discuss that, due to the nature of the AZtecCrystal algorithm, and the voting process in which child groups are reconstructed into austenite orientations, the exact position of annealing twin boundaries can be easily lost. Thus, as seen when comparing the high temperature and reconstructed EBSD maps in Fig. 3a and 3c, many twins look unreasonably reconstructed or have been missed altogether. Reconstruction accuracy could have also been impacted by the number of child orientations available per parent grain. The algorithm used by AZtecCrystal relies on a weighted voting system to select the final austenite orientations. This means that large groups (or clusters) of BCC grains will have a greater impact on the selection of the austenite orientation and the position of the austenite boundary. A smaller sample of BCC grains will therefore have less of an impact on the voting system [30].

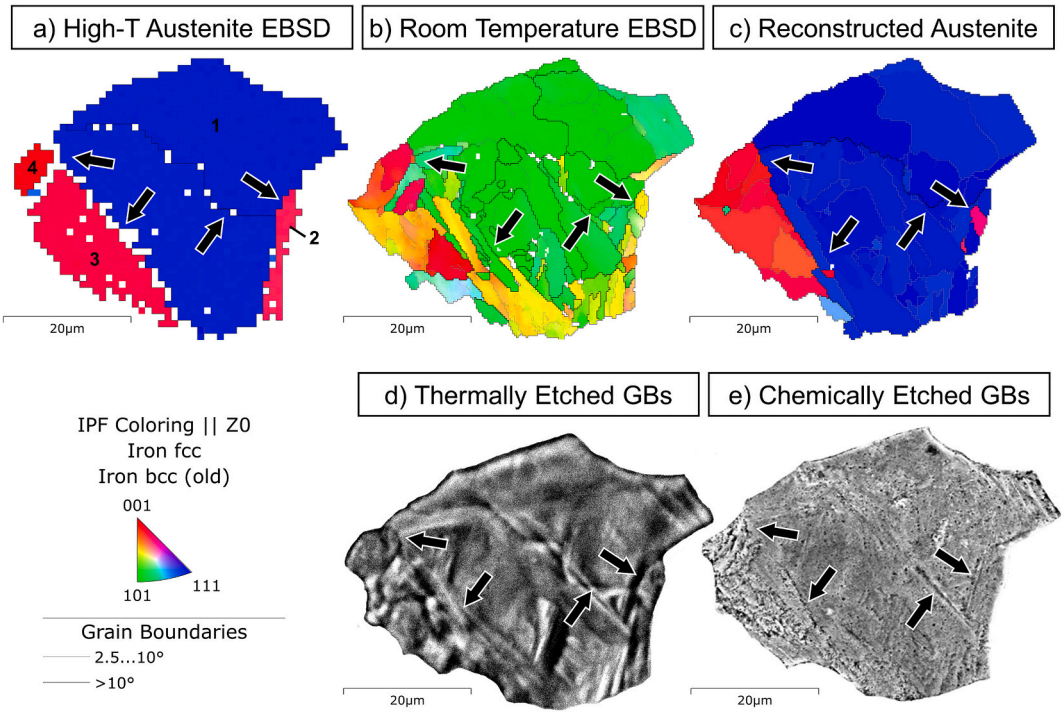

Fig. 3. A selected grain-of-interest (GOI) when viewed using (a) the 'true', high-temperature EBSD of the austenitic microstructure at the conclusion of the holding step, (b) room temperature EBSD of the BCC structure prior to cooling, (c) AZtecCrystal austenite reconstruction, (d) thermal etching, and (e) chemical etching. The annealing twins in (a) are labelled 1–4. The arrows show the position of annealing twin boundaries. EBSD data is plotted as IPF maps with grain boundaries defined by a misorientation of $> 2.5°$.

Because of crystal symmetry, accurately determining the parent grain orientation from a single child orientation is difficult, thus many unique child grains are needed within a parent grain for reconstruction to be accurate [32]. Twins 2 and 4, in the GOI, for example, do not contain a large sample size of child orientations. Thus, their weight on the voting system will have been limited and could have influenced their poorer reconstruction. An algorithm developed by Sun et al. [35] was shown to be more robust at reconstructing annealing twins. By including a "repairing" step to succeed the nucleation and growth steps of their algorithm, Sun et al. were able to adjust the ambiguous, twin-boundary regions to better resemble twinned structures. Moreover, Huang et al. [45] recently modified their algorithm described in [30] to improve reconstruction accuracy. First, they replaced their "regional voting" step with a "boundary voting" step to improve the sensitivity of the algorithm to local orientation variations. Their second change added a new "solution tuning" step to help correct any wrong reconstructions that may have occurred. Comparing this new protocol with their previous algorithm (i.e., the one used here) showed a more robust reconstruction of austenite grains and twin boundaries. At the time of writing this, this new algorithm has not been implemented into AZtecCrystal and was therefore not used in this study.

The thermally etched surface shows the presence of grooving at all four of the twin boundaries in the GOI in Fig. 3d. The thermal grooving at these boundaries, however, is not as deep or distinct as those observed at regular austenite grain boundaries. This is likely due to the free energy associated with each boundary type. Twin boundaries are more coherent than grain boundaries and therefore have a lower interfacial free energy associated with them. The matter transport mechanisms that dominate the thermal grooving process will therefore be reduced at twin boundaries, reducing the depth of the grooves and making them appear less distinct. Because of this, and the presence of the surface relief produced during the FCC-to-BCC transition, identifying these twin boundaries was made more difficult. As such, many twin boundaries were missed during the analysis of the thermally etched surface. This can be seen in Fig. 3d where the boundaries of twins 1 and 2 are slightly hidden by the presence of surface distortions. Equally, the reduced etching effect at these twin boundaries makes it difficult to distinguish between other artefacts, like ghost traces. Interestingly, twins 3 and 4 appear to be broken up by ghost traces. Observations of the growing austenite grain structure show that the GOI engulfed smaller austenite grains at the position of twins 3 and 4 (see Supplementary Gif-1). Thus, it can be concluded that these etched boundaries are traces of the previous grain structure. Consequently, the presence of these ghost traces produced a misrepresentation of the grain, and its twins, and resulted in an incorrect determination of grain boundaries.

The chemically etched surface shows negligible etching at the twin boundaries in Fig. 3e. Variations in the revealed microstructure within the GOI indicate the position of the boundaries but, without knowing they were there, it would be impossible to identify them as twin boundaries. The reduction in etching at twin boundaries is likely a consequence of a reduction in the segregation of impurities to these boundaries. Increased segregation of impurities to boundaries has been shown to improve the chemical etching effect [14]. Recent work by Herbig et al. [46] measured the variation in solute concentrations at general austenite boundaries versus annealing twin boundaries. They found that impurity solute concentrations, such as B and P, were far lower at annealing twin boundaries than at general austenite boundaries. It is therefore reasonable to assume that this difference in solute segregation is likely the reason for the decreased etching effect at twin boundaries in the SA-540 material. Because of this, most, if not all, twin boundaries were unnoticed during the analysis of the chemically etched surface. As a result, the average PAG size was greatly overestimated. Interestingly, by completely removing the twin boundaries in the high temperature EBSD map, using AZtecCrystal software, the average grain size and overall grain size distribution resembles that of the chemically etched measurements. By removing all twin boundaries, the grain size distribution of the actual grains was broadened and shifted to higher values, resulting in a measured average austenite grain size at 19.9 ±

10.3 μm, which compares closer to the measurements of the chemically etched grains. These results can be viewed in Supplementary Fig. S-4. This suggests that a lot of the disparities with the chemical etching technique were to do with its inability to reveal annealing twin boundaries. It is therefore assumed that picric etching would show an improved measurement of PAG size in a microstructure with minimal or no annealing twins.

4.2. Surface and microsegregational effects

While good indexing was achieved during the collection of EBSD maps at both high temperature and after cooling, differences in BCC orientation behaviour between the surface and the bulk were measured. EBSD measurements of the bulk BCC microstructure, shown in Supplementary Fig. S-5a, show an increased sample size of child grains, per equal area, than the surface EBSD map. The morphology of much of the surface BCC grains measured using EBSD (defined by a boundary misorientation of $>2.5°$) are globular and coarse (see Supplementary Fig. S-1), with some more lath-shaped morphologies found in enriched, interdendritic regions. Initial assessment of the BCC structure suspected this variation in morphologies to be related to the distribution of bainitic sheaves and martensitic laths. EBSD observations of the sample cross-section, however, reveal that the bulk BCC microstructure is consistently more lath-shaped in its morphology, with small fractions of coarser BCC structures. Interestingly, SE observations of the sample bulk (Supplementary Fig. S-3b) show a very similar microstructure to that observed at the surface (Supplementary Fig. S-3a). EDS measurement of the cross-section (see Supplementary Fig. S-5c) reveals that the majority of the non-lath shaped morphologies observed in the bulk BCC EBSD map are isolated to regions depleted in solute. This indicates that these coarser structures are indeed bainitic. Microhardness analysis measured an average bulk hardness of 503.6 HV, which is expected of a mixed martensite-bainite microstructure (with some autotempering), as per the authors' previous work on SA-540 [47]. To determine whether there was much discrepancy between the surface and bulk austenite microstructures, the child-BCC EBSD map of the sample bulk (Supplementary Fig. S-5a) was reconstructed into its parent-FCC microstructure (see Supplementary Fig. S-5b). The average area-weighted equivalent circle diameter of the bulk, reconstructed austenite grains (over the same size area) was measured to be 16.1 ± 11.1 μm. This value is not dissimilar to the surface reconstruction measurement (see Table 2) and indicates that the surface and bulk austenitic microstructures are indeed consistent. Moreover, EDS measurement of the bulk revealed that regions enriched in solute (i.e., interdendritic regions) also contained larger austenite grain sizes, which reflects what was seen at the surface.

The difference in EBSD results at the surface and in the bulk is unusual, especially as the microstructures are comparable under SE imaging (both show similar mixtures of martensite and bainite) and the austenitic structures are consistent. One reason for this difference could be that a preferential variant selection is occurring because of a reduction in constraint at the free surface. Without the constraint of the surrounding bulk material, independent laths, with preferential orientations, could form next to each other in groups. This would then lead to an EBSD measurement of a single, larger BCC grain instead of individual laths. The EBSD map of the BCC microstructure in Supplementary Fig. S-1b also shows the kernel average misorientation (KAM) of the surface microstructure – useful for displaying local misorientations within grains. The KAM map reveals that many of the BCC grains in the surface microstructure are broken up by bands of high misorientation. Many of these bands resemble lath boundaries, suggesting that these larger BCC grains are actually built up of multiple, smaller, similarly orientated martensitic laths. These same KAM structures are not seen to the same extent in the bulk EBSD map in Supplementary Fig. S-5a, which displays a more classical, multivariant lath structure in martensitic regions than the surface. Furthermore, the surface EBSD map shows significant texture in the BCC grains, whereas this is not reciprocated in the bulk BCC grains. Equally, a small amount of texture was also measured in the high-temperature FCC map, which could indicate that the texture in the BCC grains arose from the prior austenitic microstructure, and not variant selection, but this is difficult to determine. Pole figures showing the orientation spread of each map can be viewed in see Supplementary Fig. S-6. Nevertheless, these results give strong evidence that the surface BCC grains grew as separate laths but with similar orientations (due to variant selection), resulting in the coarse-grained map obtained. It is not fully understood why this phenomenon is more prevalent in solute depleted regions (where there are coarser BCC grains and higher densities of similar orientations) or how the formation of bainite or martensite influences it. A full explanation of these measurements is beyond the scope of this work, and an additional study dedicated to measuring this behaviour would be required for further understanding. Although there is an inconsistency between the surface and bulk EBSD maps, there is no indication that it impacted the parent reconstruction in Fig. 2c, which would rarely be conducted on the free surface (i.e., the exposed surface during heat treatment). Indeed, reducing the child misorientation threshold during reconstruction to 2.5° (see Table 1), which increased the sample size of BCC grains, was found to improve the reconstruction.

The condition of the thermally and chemically etched surfaces, prior to etching, is paramount to the accurate determination of PAG boundaries. For thermal etching, surface distortions and ghost traces made identifying the position of actual PAG and twin boundaries more difficult. Indeed, this can best seen in Fig. 3d where ghost traces misrepresented the position of actual boundaries and surface relief hid or warped the actual boundaries. Fortunately, the thermal etching achieved during this experiment was optimal. There were minimal ghost traces present and the surface distortions rarely affected the measurement of grain boundaries, although twin boundaries were harder to identify (as seen in the GOI in Fig. 3d). Work by Andres et al. [4] showed that higher austenitisation temperatures and times made ghost traces more pronounced. It was concluded that this effect was due to an increase in grain boundary mobility and deeper grooving. It can therefore be reasonably assumed that the grain boundary mobility in the SA-540 material was slow enough to avoid producing lots of ghost traces. This was likely due to the lower temperatures used during the in-situ austenitisation experiment when compared to the study by Andres et al., where ghost traces were most prevalent at temperatures above 1200 °C. Additionally, the temperature at which different alloys develop significant ghost traces will likely vary with composition. It is well know that austenite grain boundary mobility is highly dependent on the distribution of grain boundary pinning particles (GBPPs) [48], which are predominately present in micro-alloyed steels (like SA-540). Coincidentally, the presence of GBPPs could therefore make an alloy more resistant to the development ghost traces by reducing austenite boundary mobility. Furthermore, the bimodal austenite grain size distribution could be attributed to variations in GBPP equilibria across the solute segregated regions. Larger austenite grains were measured at regions enriched in Cr, Ni and Mo. This finding is counterintuitive as an enrichment in solute is expected to lead to a higher density of GBPPs and therefore a lower austenite grain size. Equilibrium phase calculations using ThermoCalc (see Supplementary Fig. S-7a) suggest that the primary GBPP for SA-540 when above the Ae_3 is AlN. The partition coefficient for Al during the solidification of SA-540 is predicted, from ThermoCalc, to be >1 (see Supplementary Fig. S-7b). This means that Al will tend to segregate in the opposite direction to other alloying elements, although this was not captured in the EDS analysis – likely due to the low composition of Al in the SA-540 material. It is therefore suggested that this potential inverse segregation of Al could be resulting in a lower density of AlN GBPPs within the interdendritic regions and produced the variations in the observed grain size.

Many regions of the chemically etched surface were etched in a way that left the matrix indistinguishable from the PAG boundaries. These regions were likely over-etched, as the remaining microstructure was

etched well and PAG boundaries were revealed. These difficulties in isolating PAG boundaries greatly reduced the accuracy of the average grain size measurement. Over-etching primarily occurred in the interdendritic regions. It is noted that the interdendritic regions are likely depleted in Al (as discussed above), however, for simplicity, these regions shall be referred to as being enriched (in relation to the partitioning of the primary alloying elements during solidification). Regions depleted in the primary alloying elements shall therefore be referred to as such. The solute variation across the sample produced variations in etching speeds between enriched and depleted zones. The enriched zones, having higher concentrations of solute, and therefore impurities, likely etched quicker than their depleted counterparts. This made balancing the level of etching between the regions difficult. As a result, the depleted regions etched well, but enriched zones were left over-etched. Further testing into the optimal concentrations of wetting agent and HCl may be required in order to reduce these effects. Additionally, tempering the material in order to induce further impurity segregation may yield more positive results.

It is unclear whether chemical microsegregation has a direct effect on the formation of thermal grooves during the thermal etching process. Thermal groove depth was sufficient for PAG analysis across both enriched and depleted regions, although surface distortions were more significant within solute enriched regions. This made the isolation of PAG boundaries, in some cases, more difficult. Notably, solute enriched regions probably transformed into their BCC structure at a lower temperature because of their higher alloying element concentrations. As a result, the volume expansion associated with these suppressed transformations would likely have been larger, thus creating larger and more visible surface distortions. Nevertheless, solute variations across the ROI did not significantly impact the reliability of the thermal etching technique.

Enriched regions of the microstructure showed a reduction in diffraction pattern quality for the given set of beam conditions and EBSD parameters. This is visualised well in the band contrast map of the BCC, room temperature EBSD in Supplementary Fig. S-1a. EBSD band contrast describes the average intensity of the measured Kikuchi bands and can be directly correlated to pattern quality. This meant that more map "cleaning" was required within lower pattern quality regions, which could lead to a reduced confidence in these results. The higher volume expansion associated with the transformations in the enriched regions of the microstructure (i.e., because of their lower transformation temperatures) will have resulted in larger residual stresses. Moreover, these same regions would have had a reduced amount of time to autotemper during cooling. These higher residual stresses can lead to a decrease in diffraction pattern quality and an increased risk of mis-indexing. Nevertheless, this behaviour can be mitigated by either improving the quality of the sample surface or by refining the beam conditions and EBSD parameters. Furthermore, for highly stressed microstructures, low temperature tempering treatments can be applied to reduce dislocation densities and relieve residual stresses without significantly altering the quenched microstructure [49].

4.3. The applicability and resilience of each technique

Both thermal etching and EBSD reconstruction yielded measurements closest to the 'true' PAG size of the analysed SA-540 material. As a PAG analysis technique, however, thermal etching is much more unreliable. The effectiveness of the technique is highly dependent on the extent of the thermal grooving achieved and the cleanliness of the surface. For low temperatures or short austenitisation times, the depth of thermal grooves may be insufficient to identify the position of PAG boundaries – making the technique redundant for investigation of many austenitisation treatments (e.g., during additive manufacturing or welding, where alloys are not held above the Ac_3 for very long). In contrast, higher austenitisation temperatures and longer austenitisation times have been shown to increase the presence of ghost traces [4], which can lead to further inaccuracies in the measurement of PAG size (as observed in the thermally etched GOI in Fig. 3d). Thermal etching is also limited to surface measurements only. Therefore, potential surface effects on grain growth could misrepresent the actual grain size in the bulk of the material. A difference between the surface and bulk BCC grains was seen when observing the microstructures as IPF maps. These differences are speculated to be caused by variant selection at the free surface (as discussed above). Differences like these begin to question whether measurements at the free surface are representative of bulk behaviour. Previous work by Andres et al. [4] noted little variation in the measured PAG size between the surface and the bulk, while assessing the thermal etching process, however supplementary work by Taylor et al. [34] showed that there was a significant difference in PAG size along their material cross-section. Mullins [6] argued that thermal grooving at the surface can result in the slowing of austenite boundary mobility and the inaccurate measurement of PAG size. Parent reconstruction of the bulk SA-540 microstructure in Supplementary Fig. S-5b, however, revealed that the surface and bulk austenite grain microstructures are consistent. Nevertheless, variations in PAG size through the sample thickness are not uncommon, as shown by [34], and should be considered when extrapolating surface measurements to bulk behaviour. Changes in constraint and mass transport, temperature and chemistry gradients, deformation caused by surface preparation or prior processing, and variations in heating and cooling rates, amongst other factors, can all influence a variation between the surface and bulk microstructures in a steel. This is a limitation of thermal etching, which is constrained to surface measurements only. EBSD and chemical etching, on the other hand, provide more freedom when selecting where to measure PAG size. Thermal etching is further complicated by the need to keep the sample surface uncontaminated. Without a sufficient vacuum or a clean environment, the polished sample surface required for thermal etching is vulnerable to oxidation and/or contamination during high temperature treatment. These factors can lead to inconsistencies in the resulting thermal etch, meaning that valuable experimental time can be wasted. Finally, although the technique can be quick (depending on the austenitisation parameters) analysis of the revealed grain boundaries can be time consuming. In this work, an average equivalent circle diameter was calculated, which required measurement of grain area. To assist with this measurement, the revealed boundaries were manually traced around to better isolate the individual grain boundaries. This step aided measurement of the PAG size but made the technique significantly more time consuming. The same step was also repeated for the chemically etched grain structure.

Chemical etching with saturated picric acid requires chemicals that are restricted in the UK. Picric acid crystals require special storing conditions and licenses, requiring labs to hold an explosives license in order to store >4 g. In addition, use of the etchant can be difficult and requires some experience. The solution must be matured with 'dummy' samples to prevent excessive attack on desired etchant surfaces. Optimal concentrations of wetting agents and HCl are dependent on the chemistry of the steel being etched [17], meaning trial-and-error studies are often required. Once the solution is prepared and matured, the method of applying etchant to the sample surface is typically swabbing rather than submersion to prevent excessive attack on the sample surface [50]. This method works well for larger samples, however, is much more difficult with smaller samples, such as the one used in this study. The level of etching during submersion can be harder to control and can increase the risk of over-etching the sample. Furthermore, a temper treatment may additionally be required to segregate impurities and improve the delineation of PAG boundaries. As with thermal etching, some grain boundaries were not fully revealed by the chemical etching process and so require manual tracing, involving some judgement of the location, of PAG boundaries. Optical micrographs are usually sufficient for this, however compounded with the over-etched surface from submersion etching, judging the lesser defined boundaries is more difficult. The improved resolution and view field of SE imaging made the

identification of the more ambiguous grain boundaries easier, however this required use of an SEM, which removes the convenience of only requiring etchant and an optical microscope.

The main drawback of parent grain reconstruction techniques are their requirement for EBSD measurement. Although EBSD detectors for electron microscopy are becoming more available, they are far less accessible than the equipment required for thermal and chemical etching techniques. The rapid EBSD detectors used in this study are rarer still. Furthermore, use of the most popular software packages for parent reconstructions requires first a purchase of a software license – e.g., AztecCrystal or MATLAB (for use of MTex software). Sufficient understanding of the reconstruction algorithms is also required for producing optimal results. Parent reconstructions can be obtained from reconstruction packages without any prior understanding, however knowledge of how best to adjust algorithm parameters is recommended in order to achieve a more accurate reconstruction. Importantly, a benefit of parent grain reconstruction algorithms is that they are always improving. For example, the main limitation of the AztecCrystal algorithm in this study was its ability to accurately reconstruct annealing twin boundaries. There have already been positive advancements in twin boundary reconstruction [35,45], which are expected to only improve as further advancements are made. Furthermore, the ability to directly compare parent EBSD data with the reconstructed microstructure of the same area (as has been demonstrated in this work) will only aid the development of reconstruction algorithms. As EBSD techniques become more accessible, and undiscovered datasets are gathered, it is an exciting time to witness how parent grain reconstruction algorithms will adapt to advancements in our fundamental understandings of steel behaviour.

5. Conclusions

The accuracy of classical PAG revealing techniques, thermal etching and picric acid etching, were compared to the more modern, parent grain reconstruction methods for measuring austenite grain size. Technique accuracy was assessed by comparison with in-situ EBSD measurements of the high temperature austenitic microstructure.

The key conclusions of this work are as follows:

1. The PAG microstructure obtained from AZtecCrystal parent grain reconstructions resulted in a more accurate measurement of austenite grain size than the other techniques especially when annealing twin boundaries were included in the measurements.
2. All PAG measurement techniques struggled with the measurement of annealing twin boundaries, which lead to many of the discrepancies between actual and revealed/reconstructed PAG measurements. Parent grain reconstructions were more consistent at recognising annealing twins, and this was improved further by refinement of the OR. The lower interfacial energy associated with twin boundaries likely lead to their irregular etching during the thermal etching process. The insufficient chemical etching observed at twin boundaries was attributed to a reduced impurity segregation to these boundaries.
3. Inherent chemical microsegregation produced a variation in the rate of chemical etching across the ROI, leading to over-etched regions and difficulties in identifying PAG boundaries. The thermal etching process appeared unaffected by solute variations, whereas a reduction in EBSD diffraction pattern quality was measured within solute enriched regions. A temper treatment may be the solution for these issues to help relieve residual stresses and improve the segregation of impurities to PAG boundaries.
4. The accessibility and resilience of each technique was discussed. The presence of ghost traces and surface relief on the thermally etched surface make the accurate isolation of PAG boundaries difficult. Chemical etching requires the use of ‘dummy’ samples and fine tuning of the technique before an optimal etch can be achieved. Although the technique requires access to EBSD measurements and reconstruction software, reconstruction accuracy has been shown to be superior to traditional techniques and is anticipated to only improve as algorithms are further optimised.
5. EBSD orientation analysis showed a high texture in the surface BCC microstructure, which was not reciprocated in the bulk, and could be indicative of variant selection, although additional work would be required to conclude this. The similarity in orientation between surface child grains originating from the same PAG made them appear coarser and less lath-like in morphology. However, this was not found to impact the EBSD reconstructions or the austenite grain size measurements between the surface and bulk. It is noted that chemical etching and EBSD techniques are not typically susceptible to such surface effects in any case.

Supplementary data to this article can be found online at https://doi.org/10.1016/j.matchar.2024.113656.

Supplementary materials

The primary Supplementary Material for this study can be viewed in the associated Supplementary Material File which can be downloaded at: https://doi.org/10.1016/j.matchar.2024.113656. Supplementary Figures include: Fig. S-1: Surface ROI EBSD maps (band contrast, IPF and KAMs) of the as-cooled BCC microstructure, Fig. S-2: EDS maps of the ROI, Fig. S-3: SE images of the surface and bulk microstructures, Fig. S-4: EBSD measurements of the ‘true’ austenite grains with annealing twin boundaries excluded, Fig. S-5: Analysis of the sample bulk, cross-section; a BCC EBSD map, a reconstructed FCC EBSD map, and a Cr EDS map of the same region, Fig. S-6: Pole figures of the surface and bulk microstructures, Fig. S-7: Thermo-Calc predictions of SA-540 equilibrium behaviour. Supplementary Gifs include: Gif S-1: Band contrast map of the in-situ, austenite grain growth of SA-540 at the ROI.

A full collection of all measured, modelled and analysed data associated with this work, has been published online on Zenodo [51] and contains: EBSD files, SE images, measured grain size lists, EDS measurements, microhardness measurements, and Thermo-Calc predictions.

CRediT authorship contribution statement

J. Collins: Writing – original draft, Visualization, Software, Methodology, Formal analysis, Data curation, Conceptualization. **M. Taylor:** Writing – original draft, Visualization, Software, Methodology, Formal analysis, Conceptualization. **A.L. Scarlett:** Writing – original draft, Methodology, Conceptualization. **E.J. Palmiere:** Writing – review & editing, Supervision, Resources. **E.J. Pickering:** Writing – review & editing, Supervision, Resources, Project administration, Funding acquisition, Conceptualization.

Declaration of competing interest

The authors declare no conflict of interest.

Data availability

The data presented in this study is openly available on Zenodo at doi:10.5281/zenodo.10469461 (accessed on 8 January 2024).

Acknowledgements

This research received financial support from Rolls-Royce plc, the EPSRC and SFI via the Centre for Doctoral Training (CDT) in Advanced Metallic Systems grants 18/EPSRC-CDT/3584 and EP/S022635/1. E. J. Pickering acknowledges the use of equipment associated with the Advanced Metals Processing and Characterisation themes of the Henry Royce Institute for Advanced Materials, funded through EPSRC grants

EP/R00661X/1, EP/S019367/1, EP/P025021/1 and EP/P025498/1. The authors would like to express thanks to Dr. Albert Smith of The University of Manchester and TESCAN UK for their support with use of the TANIST rig.

Appendix A. Appendix

The area-weighted equivalent circular diameter, $\overline{d}$, and area-weighted standard deviation, $\overline{\sigma}$, were calculated using the follow expressions

$$\overline{d} = \left(\sum_{i=1}^{n} A_i d_i\right) \Big/ \left(\sum_{i=1}^{n} A_i\right)$$

$$\overline{\sigma} = \sqrt{\left(\sum_{i=1}^{n} A_i \bullet (d_i - \overline{d})^2\right) \Big/ \left(((M-1)/M) \bullet \sum_{i=1}^{n} A_i\right)}$$

where A_i is the measured area of grain i and d_i is the calculated equivalent circle diameter (i.e., assuming the grain cross section is perfectly circular and calculating the diameter from the area) of grain i. For the calculation of the area-weighted standard deviation, M is defined as the number of none zero areas.

Appendix B. Appendix

The ASTM grain size, G, can be calculated using the methods described in ASTM Standards E112 [41] from the measured mean linear intercept, l_{int}, or from the mean planar grain diameter, d_{plan}

$$G = -3.2877 - 6.6439 \bullet log_{10} l_{int}$$

$$l_{int} = \sqrt{\pi/4} \bullet d_{plan}$$

References

[1] O.E. Hall, The deformation and ageing of mild steel: III discussion of results, Proc. Phys. Soc. B 64 (1951) 747–753.
[2] N.J. Petch, The cleavage strength of polycrystals, J. Iron Steel Inst. 174 (1953) 25–28.
[3] C. García de Andres, M.J. Bartolomé, C. Capdevila, D. San Martín, F.G. Caballero, V. López, Metallographic techniques for the determination of the austenite grain size in medium-carbon microalloyed steels, Mater. Charact. 46 (2001) 389–398.
[4] C. García de Andres, F.G. Caballero, C. Capdevila, D. San Martín, Revealing austenite grain boundaries by thermal etching: advantages and disadvantages, Mater. Charact. 49 (2003) 121–127.
[5] D. San Martí, Y. Palizdar, R.C. Cochrane, R. Brydson, A.J. Scott, Application of Nomarski differential interference contrast microscopy to highlight the prior austenite grain boundaries revealed by thermal etching, Mater. Charact. 61 (2010) 584–588, https://doi.org/10.1016/j.matchar.2010.03.001.
[6] W.W. Mullins, The effect of thermal grooving on grain boundary motion, Acta Metall. 6 (1958) 414–427.
[7] H. Pous-Romero, I. Lonardelli, D. Cogswell, H.K.D.H. Bhadeshia, Austenite grain growth in a nuclear pressure vessel steel, Mat. Sci. Eng. A 567 (2013) 72–79, https://doi.org/10.1016/j.msea.2013.01.005.
[8] C. Garcia de Andres, G. Caruana, L.F. Alvarez, Control of M23C6 carbides in 0.45C-13Cr martensitic stainless steel by means of three representative heat treatment parameters, Mat. Sci. Eng. A 241 (1998) 211–215, https://doi.org/10.1016/S0921-5093(97)00491-7.
[9] C. Sudha, A.L.E. Terrance, S.K. Albert, M. Vijayalakshmi, Systematic study of formation of soft and hard zones in the dissimilar weldments of Cr–Mo steels, J. Nucl. Mater. 302 (2002) 193–205, https://doi.org/10.1016/S0022-3115(02)00777-8.
[10] C.C. Silva, J.P. Farias, H.C. Miranda, R.F. Guimarães, J.W.A. Menezes, M.A. M. Neto, Microstructural characterization of the HAZ in AISI 444 ferritic stainless steel welds, Mater. Charact. 59 (2008) 528–533, https://doi.org/10.1016/j.matchar.2007.03.011.
[11] S. Béchet, L. Beaujard, Nouveau réactif pour la mise en évidence micrographique du grain austénitique des aciers trempés ou trempés-revenus, Rev. Met. Paris 52 (1955) 830–836, https://doi.org/10.1051/metal/195552100830.
[12] P.R. Krahe, Revealing the former austenite grain boundaries of high-purity iron-carbon alloys, Metallogr. 4 (1971) 171–175, https://doi.org/10.1016/0026-0800(71)90027-9.
[13] J.M. Capus, Austenite grain size and temper brittleness, J. Iron Steel Int. 200 (1962) 922–927.
[14] A.H. Ucisik, C.J. McMahon, H.C. Feng, The influence of intercritical heat treatment on the temper embrittlement susceptibility of aP-doped Ni-Cr steel, Metall. Trans. A. 9 (1978) 321–329, https://doi.org/10.1007/BF02646381.
[15] S. Shenhua, Y. Zexi, S. Dongdong, W. Luqian, Effects of phosphorus grain boundary segregation and hardness on the ductile-to-brittle transition for a 2.25Cr1Mo steel, J. Wuhan Univ. Technol. Mater. Sci. Ed. 22 (2007) 1–6, https://doi.org/10.1007/s11595-005-1001-x.
[16] R. Thackray, E.J. Palmiere, O. Khalid, Novel etching technique for delineation of prior-austenite grain boundaries in low, medium and high carbon steels, Mater. 13 (2020) 3296, https://doi.org/10.3390/ma13153296.
[17] K.F. Rodriguez-Galeano, L.F. Romano-Acosta, E.J. Palmiere, W.M. Rainforth, A new approach to etching low-carbon microalloyed steels to reveal prior austenite grain boundaries and the dual-phase microstructure, J. Microsc. 289 (2023) 73–79, https://doi.org/10.1111/jmi.13153.
[18] D.R. Barraclough, Etching of prior austenite grain boundaries in martensite, Metallog. 6 (1973) 465–472, https://doi.org/10.1016/0026-0800(73)90044-X.
[19] M. Pereira-da-Silva, F.A. Ferri, in: A.L. Da Róz, M. Ferreira, F. Leite, O.N. Oliveira (Eds.), Scanning Electron Microscopy, Nanocharacterization Techniques, William Andrew, 2017, pp. 1–35.
[20] M. Humbert, H. Moustahfid, F. Wagner, M.J. Philippe, Evaluation of the high temperature texture of the β phase of a TA6V sample from the individual orientations of grains of the low temperature α phase, Scr. Mater. 30 (1994) 377–382.
[21] C. Cayron, Reconstruction of parent grains from EBSD data, Mater. Charact. 57 (2006) 386–401, https://doi.org/10.1016/j.matchar.2006.03.008.
[22] G. Kurdjumov, G. Sachs, Über der Mechanismus der Stahlhärtung, Z. Phys. 64 (1930) 325–343.
[23] Z. Nishiyama, X-ray investigation of the mechanism of the transformation from face centred cubic lattice to body centred cubic, Sci. Rep. Tohoku Univ. 23 (1934) 637.
[24] O. Instruments, AztecCrystal, Available online: https://nano.oxinst.com/azteccrystal, 2023 (accessed on 30 October 2023).
[25] MTEX, MTEX, Available online: https://mtex-toolbox.github.io/index, 2023 (accessed on 30 October 2023).
[26] E. Gomes, L.A.I. Kestens, Fully automated orientation relationship calculation and prior austenite reconstruction by random walk clustering, IOP Conf. Series: Mater. Sci. Eng. 82 (2015) 012059, https://doi.org/10.1088/1757-899X/82/1/012059.
[27] A. Brust, E. Payton, T. Hobbs, V. Sinha, V. Yardley, S. Niezgoda, Probabilistic reconstruction of austenite microstructure from Electron backscatter diffraction observations of Martensite, Microsc. Microanal. 27 (2021) 1035–1055, https://doi.org/10.1017/S1431927621012484.
[28] E. Gomes de Araujo, H. Pirgazi, M. Sanjari, M. Mohammadi, L.A.I. Kestens, Automated reconstruction of parent austenite phase based on the optimum orientation relationship, J. Appl. Crystallogr. 54 (2021) 569–579, https://doi.org/10.1107/S1600576721001394.
[29] L. Germain, N. Gey, R. Mercier, P. Blaineau, M. Humbert, An advanced approach to reconstructing parent orientation maps in the case of approximate orientation relations: application to steels, Acta Mater. 60 (2012) 4551–4562, https://doi.org/10.1016/j.actamat.2012.04.034.
[30] C.-Y. Huang, H.-C. Ni, H.-W. Yen, New protocol for orientation reconstruction from martensite to austenite in steels, Materialia 9 (2020) 100554, https://doi.org/10.1016/j.mtla.2019.100554.

[31] R. Hielscher, T. Nyyssönen, F. Niessen, A.A. Gazdar, The variant graph approach to improved parent grain reconstruction, Materialia 22 (2022) 101399, https://doi.org/10.1016/j.mtla.2022.101399.
[32] F. Niessen, T. Nyyssönen, A.A. Gazdar, R. Hielscher, Parent grain reconstruction from partially or fully transformed microstructures in MTEX, J. Appl. Crystallogr. 55 (2022) 180–194, https://doi.org/10.1107/S1600576721011560.
[33] G. Miyamoto, N. Iwata, N. Takayama, T. Furuhara, Mapping the parent austenite orientation reconstructed from the orientation of martensite by EBSD and its application to ausformed martensite, Acta Mater. 58 (2010) 6393–6403, https://doi.org/10.1016/j.actamat.2010.08.001.
[34] M. Taylor, A.D. Smith, J.M. Donoghue, T.L. Burnett, E.J. Pickering, In-situ heating-stage EBSD validation of algorithms for prior-austenite grain reconstruction in steel, Scr. Mater. 242 (2024) 115924, https://doi.org/10.1016/j.scriptamat.2023.115924.
[35] D. Sun, Z. Zhou, K. Zhang, X. Yang, X. Liu, Z. Guo, J. Gu, Novel reconstruction approaches of austenitic annealing twin boundaries and grain boundaries of ultrafine grained prior austenite, Mater. Des. 227 (2023) 111692, https://doi.org/10.1016/j.matdes.2023.111692.
[36] D. Sun, C. Li, X. Xue, Y. Liu, Z. Guo, J. Gu, Optimization scheme of the orientation relationship from crystallographic statistics of variants and its application to lath martensite, Mater. Des. 195 (2020) 109022, https://doi.org/10.1016/j.matdes.2020.109022.
[37] SciPy, SciPy, Available online: https://scipy.org, 2023 (accessed on 30 October 2023).
[38] scikit-Image Image Processing in Python. scikit-Image, Available online: https://scikit-image.org, 2023 (accessed on 30 October 2023).
[39] J. Collins, Grain Image Analysis, Available online: https://github.com/JoshUoM/grain_image_analysis, 2023 (accessed on 31 October 2023).
[40] N. Bozzolo, M. Bernacki, Viewpoint on the formation and evolution of annealing twins during thermomechanical processing of FCC metals and alloys, Metall. Mater. Trans. A 51A (2020) 2665–2684, https://doi.org/10.1007/s11661-020-05772-7.
[41] Standard Test Methods for Determining Average Grain Size, ASTM International, West Conshohocken, PA, USA, 2010.
[42] E.E. Underwood, Surface area and length in volume, in: R.T. DeHoff, F.N. Rhines (Eds.), Quantitative Microscopy, McGraw-Hill, 1968, pp. 77–127.
[43] N. Nakada, T. Tsuchiyama, S. Takaki, S. Hashizume, Variant selection of reversed austenite in lath Martensite, ISIJ Int. 47 (2007) 1527–1532.
[44] S.K. Giri, A. Durgaprasad, K.V. Manikrishna, C.R. Anoop, S. Kundu, I. Samajdar, Exploring the origin of variant selection through martensite-austenite reconstruction, Philos. Mag. 99 (2019) 699–717, https://doi.org/10.1080/14786435.2018.1552030.
[45] C.-Y. Huang, S.-L. Lu, H.-W. Yen, Digital reconstruction of engineered austenite: revisiting effects of grain size and Ausforming on variant selection of Martensite, Metals 12 (2022) 1511, https://doi.org/10.3390/met12091511.
[46] M. Herbig, M. Kuzmina, C. Haase, R.K.W. Marceau, I. Gutierrez-Urrutia, D. Haley, D.A. Molodov, P. Choi, D. Raabe, Grain boundary segregation in Fe–Mn–C twinning-induced plasticity steels studied by correlative electron backscatter diffraction and atom probe tomography, Acta Mater. 83 (2015) 37–47, https://doi.org/10.1016/j.actamat.2014.09.041.
[47] J. Collins, M. Piemonte, M. Taylor, J. Fellowes, E. Pickering, A. Rapid, Open-source CCT predictor for low-alloy steels, and its application to compositionally heterogeneous material, Metals 13 (2023) 1168, https://doi.org/10.3390/met13071168.
[48] T. Gladman, The Physical Metallurgy of Microalloyed Steels Chapter 4, Institute of Materials, London, UK, 1997, pp. 137–183.
[49] W. Zheng, J. Zhu, W. Yuan, Tempering stress relaxation behavior and microstructure evolution of 300 M steel, Mater. Charact. 197 (2023) 112688, https://doi.org/10.1016/j.matchar.2023.112688.
[50] G.F. Vander Voort, Revealing prior-austenite grain boundaries, Microsc. Microanal. 16 (2010) 774–775, https://doi.org/10.1017/S1431927610053973.
[51] J. Collins, M. Taylor, A.L. Scarlett, E.J. Palmiere, E.J. Pickering, Supplementary material for "Prior Austenite Grain Measurement: A Direct Comparison of EBSD Reconstruction, Thermal Etching and Chemical Etching", Zenodo, 2024 https://doi.org/10.5281/zenodo.10469461 (Version v1) [Data set].